

Rare-Earth vs. Heavy Metal Pigments and their Colors from First Principles

Jan M. Tomczak,¹ L. V. Pourovskii,² L. Vaugier,² A. Georges,^{2,3,4,5} and S. Biermann^{2,5}

¹*Department of Physics and Astronomy, Rutgers University, Piscataway, New Jersey 08854, USA*

²*Centre de Physique Théorique, Ecole Polytechnique, CNRS UMR7644, 91128 Palaiseau, France*

³*Collège de France, 11 place Marcelin Berthelot, 75005 Paris, France*

⁴*DPMC-ManEP, Université de Genève, 24 quai Ernest Ansermet, CH-1211 Genève, Suisse*

⁵*Japan Science and Technology Agency, CREST, Kawaguchi 332-0012, Japan*

PACS numbers:

Many inorganic pigments contain heavy metals hazardous to health and environment. Much attention has been devoted to the quest for non-toxic alternatives based on rare-earth elements. The computation of colors from first principles is a challenge to electronic structure methods however, especially for materials with localized *f*-orbitals. Here, starting from atomic positions only, we compute the color of the red pigment cerium fluorosulfide CeSF, as well as of mercury sulfide HgS (classic ‘vermilion’). Our methodology employs many-body theories to compute the optical absorption, combined with an intermediate length-scale modelization to assess how coloration depends on film thickness, pigment concentration and granularity. We introduce a quantitative criterion for the performance of a pigment. While for HgS this criterion is satisfied due to large transition matrix elements between wide bands, CeSF presents an alternative paradigm: the bright red color is shown to stem from the combined effect of the quasi two-dimensionality and the localized nature of *4f* states. Our work demonstrates the power of modern computational methods, with implications for the theoretical design of materials with specific optical properties.

Light propagating inside a heterogeneous solid experiences (i) absorption, and (ii) scattering. The light that is not absorbed is diffusely reflected and is responsible for the perceived color. The visual appearance of a material is hence determined by *selective absorption of light* and *sufficient (back)scattering*. For a material to be e.g. a luminous red pigment, two criteria must thus be satisfied. First, its absorption edge should be located at the appropriate energy (~ 2.1 eV) so that the red component of the visible spectrum is not absorbed. Second, the absorption edge should be sharp, so that most other photons within the visible range (green, blue) are absorbed.

The computation of these effects from first principles is faced with three fundamental difficulties. First, in view of the sensitivity of the human eye, the optical gap must be obtained with a precision of at least 100 meV. Conventional electronic structure methods yield a well-

documented underestimation of the gap of conventional semiconductors. Second, the localized *4f* states, which play a crucial role in optical properties of rare-earth based pigments[1–3], are poorly described by standard density-functional theory[4] or even *GW* approaches[10]. Third, a realistic assessment of the coloration of a pigment must take into account scattering properties depending on concentration, granularity and film thickness. *Ab initio* simulations so far have not ventured beyond calculating the optical conductivity of infinite bulk samples (see however Ref. [6, 7] for organic molecules). In this article we address all these issues and develop a general methodology for the prediction of the color of narrow-band materials.

We investigate cerium fluorosulfide (CeSF), a typical example of the new class of rare-earth pigments [5, 28]. It crystallizes in the layered ThCr_2Si_2 structure sketched in Fig. 1 (which is incidentally also that of the recently discovered iron-based superconductors [10]). The same figure displays the momentum-dependent many-body spectral function $A_{\mathbf{k}}(\omega)$ that encodes the excitation energies associated with the addition or removal of an electron into the many-body ground-state (see Supporting Information). The localized Ce-*4f* states form quasi-atomic multiplets that hybridise weakly with the rest of the solid. From the panels (c)–(e), displaying the specific orbital character of each electronic state, it is apparent that the top of the valence band has dominantly S-3p character. The occupied Ce-*4f* states are located at higher binding energies, near the center of the S-3p bands. The lowest unoccupied states are found to be the almost localized empty Ce-*4f* states, with the dispersing Ce-5d conduction band lying higher in energy.

The calculated optical gap $\Delta = 2.14$ eV (578 nm) is consistent with the red color of this material. Furthermore, our calculation reveals that the absorption edge is associated with the optical transition between S-3p states and Ce-*4f* states. This is at variance with the standard lore associating the coloration of cerium-based pigments to the intra-atomic Ce-*4f* to Ce-5d transition. Indeed, such a conventional assignment was proposed for CeSF in Ref. [5], and X-ray photoemission spectra (XPS) were interpreted along the same lines in Ref. [11]. In figure 2, we show that our results are nonetheless fully consistent with

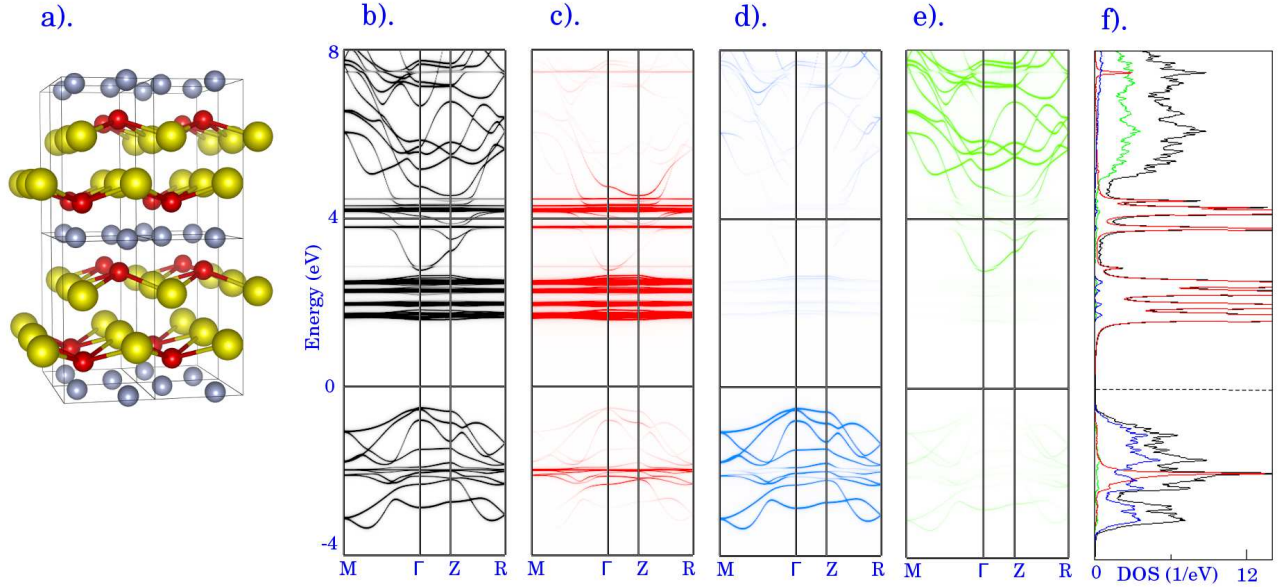


FIG. 1: **Cerium fluorosulfide CeSF.** a) Crystal structure. The red, yellow and grey spheres represent Ce, S, and F, respectively. b). The total many-body momentum-dependent spectral function $A_{\mathbf{k}}(\omega)$ along high symmetry lines. c-e). The corresponding partial spectral functions for Ce 4f (c), S 3p(d), and Ce 5d(e). f). The total momentum-integrated spectral function (black curve) as well as the partial momentum-integrated spectral functions for Ce 4f (red), S 3p (blue) and Ce 5d (green).

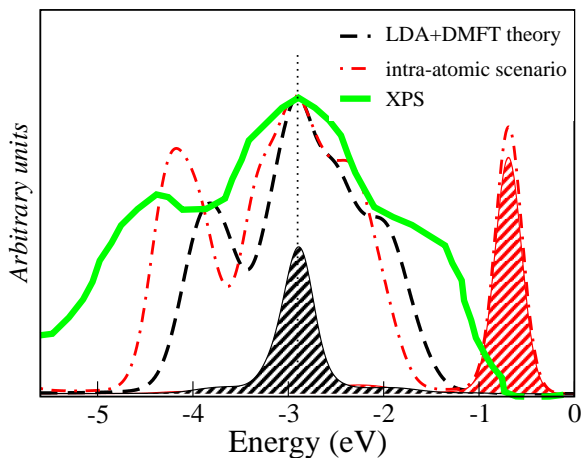


FIG. 2: **X-ray photoemission spectroscopy (XPS).** The many-body spectral momentum-integrated function (black curve) of CeSF compared to experimental XPS spectra [11] (thick green curve). In order to simulate experimental resolution the theoretical spectral function has been convoluted with a Gaussian of full width at half maximum of 0.3 eV. As a comparison we show (red curve) the XPS spectrum of the alternative intra-atomic scenario previously proposed [See the text and Supporting Information for a discussion]. The shaded regions of the corresponding colors are the contribution from Ce 4f states in each case.

assignment of the observed spectral peaks: according to our calculations, the peak at -3 eV is due to contributions from localized Ce 4f states while the shoulder at -1.5eV is mainly formed by S-3p states that are pushed upwards in energy by the hybridization with Ce-4f states. The previously proposed ‘intra-atomic’ scenario can also be simulated theoretically (see Supporting Information) and is shown in Fig. 2 to be inconsistent with the measured spectra.

In contrast to CeSF, mercury sulfide α -HgS (also known as cinnabar red or “vermillion”) has been used as a red pigment since antiquity [12]. It is a conventional semiconductor with a simple hexagonal structure. Although the additional complication of localized states is not present here, an accurate determination of the gap requires the use of GW calculations (see Supporting Information for details). The onset of absorption is due to transitions between broad and strongly hybridizing bands of mainly S-3p and Hg-6s character. Given the qualitatively different nature of the optical transitions involved, HgS and CeSF are good pigments for entirely different reasons, as explained in detail below.

The absorption properties of these two compounds can be derived from the frequency-dependent optical conductivity, $\text{Re } \sigma(\omega)$. Using linear response theory, and neglecting excitonic effects (see the Supporting Information

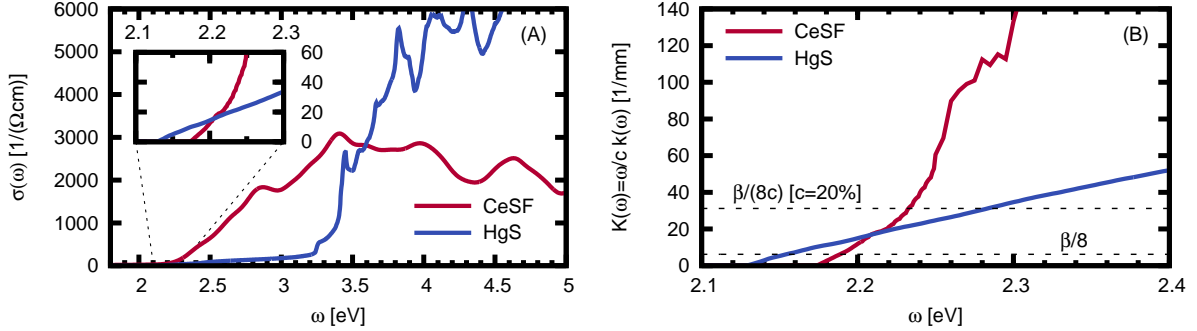


FIG. 3: **Optical conductivity and absorption coefficient of CeSF and HgS.** (A) Polarization averaged optical conductivity. The inset is a zoom into the energy region of the onset of absorption. (B) Macroscopic absorption coefficient K . The horizontal dashed lines are the quality criterion (3) as defined in the text computed for $\beta = 50/\text{mm}$.

for a discussion), it can be expressed as (see e.g. [13, 14]):

$$\text{Re } \sigma_\alpha(\Omega) = \frac{2\pi e^2}{V\hbar} \sum_{\mathbf{k}} \int d\omega \frac{f(\omega) - f(\omega + \Omega)}{\Omega} \times \text{tr} \left\{ A_{\mathbf{k}}(\omega + \Omega) \hbar v_{\mathbf{k},\alpha} A_{\mathbf{k}}(\omega) \hbar v_{\mathbf{k},\alpha} \right\} \quad (1)$$

where V is the unit-cell volume, α labels the polarization, $v_{\mathbf{k},\alpha}$ are the optical transition matrix elements and the Fermi functions $f(\omega)$ restrict transitions to take place between occupied and empty states. The absorption is described by the *macroscopic* absorption coefficient $K(\omega)$:

$$K(\omega) = \frac{\omega}{c_e} k(\omega) = \frac{\omega}{c_e} \text{Im} \sqrt{1 + \frac{4\pi i}{\omega} \sigma(\omega)} \quad (2)$$

where $k(\omega)$ is the imaginary part of the refractive index, and c_e the speed of light.

The calculated optical conductivity and absorption coefficient of CeSF and α-HgS are displayed in Fig. 3(a),(b). While marked differences exist between the two compounds on a broad energy range, the magnitude of σ and K near the onset of absorption (see the inset of figure 3(a) and figure 3(b)) is actually similar, with $\sigma \simeq 50 \Omega^{-1}\text{cm}^{-1}$ and $K \simeq 20\text{mm}^{-1}$ for $\omega = \Delta + 0.1 \text{ eV}$. The physical origin of the spectral weight just above the absorption edge (which in turn determines K) is however fundamentally different for HgS and CeSF. Indeed we will now show that the large absorption in HgS is due to the strength of optical transition matrix elements, while for CeSF it is due to the large density of localized Ce-4f as well as weakly dispersing S-3p states.

To substantiate this claim, we note that color is determined by a fairly small frequency range above the absorption edge (see also below), and, hence, we focus on $\Delta \lesssim \hbar\omega \lesssim \Delta + \hbar\delta\omega_c$, with $\hbar\delta\omega_c \approx 0.2 \text{ eV}$. In order to disentangle density of states effects from transition probabilities, we compute the ratio between the optical conductivity, equation (1), and the joint density of states $N(\omega)$ [31] at the energy $\omega = \Delta + \hbar\delta\omega_c$.

We find that $\sigma/N = 2.5 (\hbar/(a_0 m_e))^2$ for HgS, while $\sigma/N = 0.86 (\hbar/(a_0 m_e))^2$ is almost three times smaller for CeSF (a_0 is the Bohr radius and m_e the mass of the electron). This proves that transition matrix elements dominate for HgS, while density of states effects dominate for CeSF. The reason for this is the weak dispersion of the Ce-4f states (expected from their localized character), but also of the S-3p states at the top of the valence band in CeSF. Interestingly, the weak dispersion of the S-3p states along the *c*-axis is due to the quasi two-dimensional environment of the sulfur atoms, which are located within layers parallel to those containing cerium atoms (Fig. 1(a)). As detailed in the Supporting Information, the joint density of states $N(\omega)$ and the absorption $K(\omega)$ display a discontinuous increase at threshold $N \propto \theta(\hbar\omega - \Delta)$ for a strictly two-dimensional dispersion. In contrast, a three-dimensional parabolic dispersion (mimicking e.g. the 3p or 6s bands in HgS) yields a less sharp frequency-dependence $\propto (\hbar\omega - \Delta)^{1/2}$ above the absorption edge.

The macroscopic quantities σ and K describe the absorption properties of a perfectly crystalline bulk solid. Pigments are used however (in e.g. paints) in the form of small particles embedded into a transparent matrix. In this context, light propagation depends on the morphology of the sample, and a multiple scattering problem has to be solved to determine the *diffuse reflectance* $R(\omega)$ (in contrast to the simpler specular reflectivity [29, 30]). A commonly used [35] approach is the effective-medium description due to Kubelka and Munk (KM) [32, 34]. The KM model treats the propagation of light through a homogeneous layer of matter with pigment concentration c , that absorbs light with rate $cK(\omega)$ and backscatters with rate $\beta(\omega)$ per unit length. The quantity β effectively contains all the information on the microscopic structure of the sample. As shown in the Supporting Information, the energy dependence of β can be neglected, and we use a typical value $\beta = 50\text{mm}^{-1}$, consistent with the range of values $\beta \approx 10 - 500\text{mm}^{-1}$

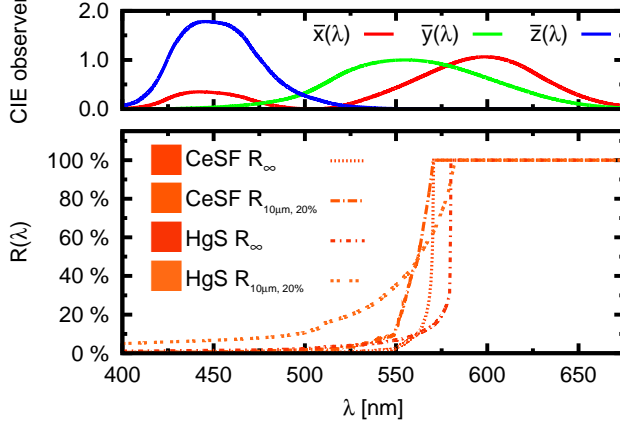


FIG. 4: Diffuse reflectance and the colors Top: color-matching functions \bar{x} , \bar{y} , \bar{z} of the human eye (CIE 1931 XYZ standard) as a function of wavelength λ (see also Supporting Information). Bottom : calculated diffuse reflectances of CeSF and HgS. Shown are the diffuse reflectances of the bulk (R_∞) and of a diluted (concentration 20%) thin film of $10\mu\text{m}$ on a white substrate ($R_{10\mu\text{m}, 20\%}$) computed for $\beta = 50 \text{ mm}^{-1}$. The corresponding color for each case is displayed in the legend).

reported in the literature for a wide range of industrial inorganic pigments [35]. For a semi-infinite layer, the KM model yields a simple expression for the diffuse reflectance: $R_\infty(\omega) = \alpha(\omega) - \sqrt{\alpha(\omega)^2 - 1}$, with $\alpha(\omega) = 1 + 2cK(\omega)/\beta(\omega)$. As expected, $R_\infty \approx 1$ for $cK/\beta \ll 1$ (weak absorption) and $R_\infty \approx 0$ for $cK/\beta \gg 1$ (strong absorption). The formula for a sample of finite thickness is given in the Supporting Information.

We have employed the KM model in conjunction with our first-principles absorption $K(\omega)$ to compute the diffuse reflectance of CeSF and HgS samples, as well as their color (Fig. 4). The latter is obtained (e.g. as XYZ tristimulus values or xy chromaticities) by taking into account the spectral distribution of the light source as well as the sensitivity of the human eye to red, green and blue light as encoded in the empirical color matching functions displayed in the top panel of Fig. 4 (for details, see Supporting Information). We considered semi-infinite samples as well as realistic $10\mu\text{m}$ layers on a white ($R=1$) substrate, consisting of either pure ($c = 100\%$) or diluted ($c = 20\%$) pigments. The resulting diffuse reflectances and colors depicted in Fig. 4 reveal that the pure semi-infinite bulk samples of both materials have bright red colors, while the thin films with a pigment concentration of 20% have a more orange tone, especially for HgS.

We now introduce a simple performance criterion for the usability of such materials as pigments. In order for the color to be a bright red, the reflectance for $\omega > \Delta$ should drop sufficiently quickly such that admixtures from the green and blue part of the visible spectrum are suppressed. This can be insured by requiring that $R(\Delta + \hbar\delta\omega_c) \leq 1/2$. Here, $\hbar\delta\omega_c \approx 0.2\text{eV}$ is the characteristic frequency interval over which the human eye distinguishes between the primary colors (corresponding to

$\delta\lambda \approx 60\text{nm}$ for red light, see top panel of Fig. 4). Since the reflection for $\omega > \Delta$ arises from a finite absorption, the above requirement can be translated, using the KM model, into the criterion:

$$K(\Delta + \hbar\delta\omega_c) \stackrel{!}{\geq} \beta/(8c) \quad (3)$$

This threshold is marked in figure 3(b): for pure materials ($c = 100\%$) both CeSF and HgS largely satisfy the criterion. Indeed, $R_\infty(\lambda)$ with $\beta = 50\text{mm}^{-1}$ switches from $R_\infty = 0$ to $R_\infty = 1$ within only a few nanometers (Fig. 4). Criterion (3) can be turned, for a given c/β , into a minimal thickness L_{min} above which the pigment has the same apparent color as the bulk, i.e. its color is sufficiently stable. This is represented in Fig. 5. Using $\beta = 50/\text{mm}$, the minimal thickness of a paint layer consisting of 20% CeSF is $3.2\mu\text{m}$, whereas it is $35\mu\text{m}$ for 20% HgS. As a result, the reflectivity of $10\mu\text{m}$ layers with 20% diluted HgS violates our quality criterion, which explains the notably different (orange) color of those samples, observed in figure 4.

In conclusion, we presented a framework for the theoretical determination of the color of pigment materials. Our methodology combines first-principles calculations of the frequency-dependent absorption based on state-of-the art many-body theories, with an intermediate length-scale modelization of the scattering properties of realistic samples. We applied this methodology to classic ‘vermillion’ HgS and to the recently discovered rare-earth pigment CeSF. Our results reveal that the red coloration of these two materials has a very different origin at the atomic scale. While it is due to large optical matrix elements in HgS, the key effect in CeSF is the large density of weakly dispersing states (resulting both from the low-dimensionality of the crystal structure and the localized

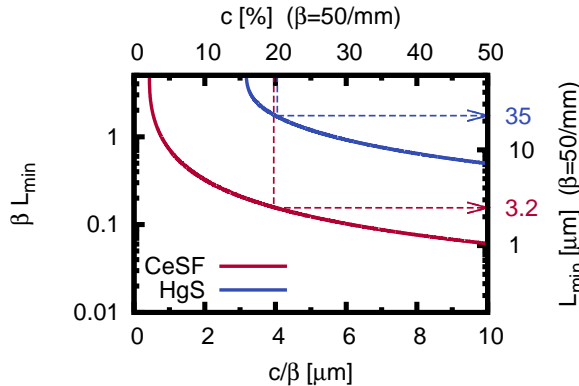


FIG. 5: Universal quality curves for thin films of CeSF and HgS. The thin films located above the corresponding curve in the $(\beta L_{min}, c/\beta)$ coordinates pass the quality criterion for a good pigment (see the text). The top and right axes correspond to a fixed value of β of 50/mm, allowing for a direct translation of a given concentration into a minimal film thickness.

character of Ce 4f states). We also demonstrated that the relevant optical transitions in CeSF are S-3p to Ce-4f inter-atomic transitions, in contrast to previous belief. Our methodology may lead to rational materials design in which first-principles calculations are used in synergy with solid-state chemistry in order to create new materials with specific optical properties.

METHODS

Combining electronic structure and many-body techniques [1, 2, 4, 9, 20–22] we calculate the electronic structure of rare-earth pigments. Then we take these approaches further by performing an *ab initio* calculation of the optical response functions and going all the way to a prediction of the actual color (expressed e.g. in RGB coordinates [38, 39]) of a sample with a given granularity, using an intermediate length-scale modelisation [32].

As discussed in the main text, the strong Coulomb repulsion between the 4f electrons in CeSF is responsible for the splitting between the empty Ce-4f states at the bottom of the conduction band and the occupied Ce-4f states, which hybridise with the S-3p states to form the valence band. A proper treatment of this strong Coulomb interaction is essential in order to correctly reproduce the optical gap and electronic structure of this material. Hence, we have employed the so-called LDA+DMFT approach[21, 22], which combines electronic structure calculations with a many-body treatment of local correlations on the Ce 4f shell in the framework of dynamical mean-field theory (DMFT) [20]. The interaction vertex has been computed from first principles using the constraint random phase approximation[6, 7].

Within LDA+DMFT, the Ce-4f shell is treated as that of an effective atom, self-consistently coupled to an environment describing the rest of the solid. From the Hamiltonian of this effective atom (which takes into account crystal-field effects, intra-atomic Coulomb interactions and the spin-orbit

coupling), a many-body self-energy is computed and inserted into the Green's function of the full solid. Self-consistency over the total charge density and the effective atom parameters is implemented [1, 4]. Important technical points of our calculational approach are presented in the Supporting Information.

We are grateful to Erich Wimmer and René Windiks, who introduced us to the field of rare-earth-based pigments, and acknowledge useful discussions with David Jacobs and Hong Jiang. This work was supported by the French ANR under projects CorrelMat and SURMOTT, by the NSF materials world network under Grant NSF DMR 0806937, as well as by IDRIS/GENCI under project 1393.

author contributions J. M. T. and L. P. performed the calculations of the electronic structure and optical spectra. L. V. performed the calculations of the screened Coulomb interactions. S. B. and A. G. provided guidance and coordinated the project. All authors contributed to the analysis and discussion of the results, and to the writing of the article.

-
- [1] Berte JN (2002) *in High Performance Pigments*, ed Smith HM (Wiley-VCH), pp 27–40.
 - [2] Jansen M, Letschert HP (2000) Inorganic yellow-red pigments without toxic metals. *Nature* 404:980–982.
 - [3] Maestro P, Huguenin D (1995) Industrial applications of rare earths: which way for the end of the century. *J. Alloys Comp.* 225:520–528.
 - [4] Kohn W (1999) Nobel Lecture: Electronic structure of matter-wave functions and density functionals. *Rev. Mod. Phys.* 71(5):1253–1266.
 - [5] Aryasetiawan F, Gunnarsson O (1998) The GW method. *Rep. Prog. Phys.* 61:237–312.
 - [6] Malcioglu OB, Calzolari A, Gebauer R, Varsano D, Baroni S (2011) Dielectric and thermal effects on the optical properties of natural dyes: A case study on solvated cyanin. *Journal of the American Chemical Society* 133:15425–15433.
 - [7] Wanko M, García-Risueño P, Rubio A (2012) Excited states of the green fluorescent protein chromophore: Performance of ab initio and semi-empirical methods. *Phys. Status Solidi B* 249:392–400.
 - [8] Demourgues A, Tressaud A, Laronze H, Macaudiere P (2001) Rare earth fluorosulfides LnSF and Ln₂AF₄S₂ as new colour pigments. *J. Alloys and Comp.* 323–324:223–230.
 - [9] Goubin F, et al. (2004) The dielectric function of LnSF rare-earth fluorosulfides (Ln = La, Ce): experiment and theory. *J. Solid State Chem.* 117:2833–2840.
 - [10] Kamihara Y, Watanabe T, Hirano M, Hosono H (2008) Iron-based layered superconductor La[O_{1-x}F_x]FeAs (x = 0.05–0.12) with T_c = 26K. *J. Am. Chem. Soc.* 130:3296–3297.
 - [11] Pauwels D (2003) Cristallochimie des composés de terres rares à anion mixtes. Propriétés d'absorption UV-visible [Structural features of rare earth-based mixed anions compounds (O, S, F); UV-Visible absorption properties] Ph.D. thesis (L'Université Bordeaux I, Bordeaux). French.
 - [12] Gettens RJ, Feller RL, Chase WT (1993) *in Artists' Pigments: A Handbook of Their History and characteristics*,

- Vol. 2, ed Roy A (Oxford University Press, Oxford), pp 159–182.
- [13] Millis AJ (2004) *Optical Conductivity and Correlated Electron Physics* ed D. Baeriswyl LD (Physics and Chemistry of Materials with Low-Dimensional Structures), Vol. 25, p 195ff.
- [14] Tomczak JM, Biermann S (2009) Optical properties of correlated materials: Generalized peierls approach and its application to VO₂. *Phys. Rev. B* 80:085117
- [15] Tomczak JM, Biermann S (2009) Optical properties of correlated materials - or why intelligent windows may look dirty. *Phys. Status Solidi B (feature article)* 246:1996
- [16] Tomczak JM, Biermann S (2009) Materials design using correlated oxides: Optical properties of vanadium dioxide. *Europhys. Lett.* 86:37004
- [17] Levinson R, Berdahl P, Akbari H (2005) Solar spectral properties of pigments, part ii. *Solar Ener. Mat. Solar Cells* 89:351–389.
- [18] Kubelka P (1948) New contributions to the optics of intensely light-scattering materials, part I. *J. Opt. Soc. Am.* 38:448–457.
- [19] Levinson R, Berdahl P, Akbari H (2005) Solar spectral properties of pigments, part I. *Solar Ener. Mat. Solar Cells* 89:319–349.
- [20] Georges A, Kotliar G, Krauth W, Rozenberg MJ (1996) Dynamical mean-field theory of strongly correlated fermion systems and the limit of infinite dimensions. *Rev. Mod. Phys.* 68:13–125.
- [21] Anisimov VI, Poteryaev AI, Korotin MA, Anokhin AO, Kotliar G (1997) First-principles calculations of the electronic structure and spectra of strongly correlated systems: dynamical mean-field theory. *J. Phys.: Condens. Matter* 9:7359.
- [22] Lichtenstein AI, Katsnelson MI (1998) Ab initio calculations of quasiparticle band structure in correlated systems: LDA++ approach. *Phys. Rev. B* 57:6884–6895.
- [23] Pourovskii LV, Amadon B, Biermann S, Georges A (2007) Self-consistency over the charge-density in dynamical mean-field theory: a linear muffin-tin implementation and some physical implications. *Phys. Rev. B* 76:235101.
- [24] Aichhorn M, et al. (2009) Dynamical mean-field theory within an augmented plane-wave framework: Assessing electronic correlations in the iron pnictide LaFeAsO. *Phys. Rev. B* 80:085101.
- [25] Aichhorn M, Pourovskii L, Georges A (2011) Importance of electronic correlations for structural and magnetic properties of the iron pnictide superconductor LaFeAsO. *Phys. Rev. B* 84:054529.
- [26] Ferrero, M, Parcollet, O TRIQS: a Toolbox for Research in Interacting Quantum Systems. <http://ipht.cea.fr/triqs>.
- [27] CIE (1932) *Commission internationale de l'Eclairage proceedings [Proceedings of the International Commission on Illumination]*, 1931 (Cambridge University Press, Cambridge). French.
- [28] Smith T, Guild J (1931) The C.I.E. colorimetric standards and their use. *Transactions of the Optical Society* 33:73–134.
- [29] Aryasetiawan F, et al. (2004) Frequency-dependent local interactions and low-energy effective models from electronic structure calculations. *Phys. Rev. B* 70:195104.
- [30] Vaugier L, Jiang H, Biermann S (2012) Hubbard *U* and Hund's exchange *J* in transition metal oxides: Screening vs. localization trends from constrained random phase approximation. *Phys. Rev. B* 86:165105.
- [31] obtained from replacing the trace in equation (1) with $\text{tr}\{A_{\mathbf{k}}(\omega + \Omega)\} / \text{tr}\{A_{\mathbf{k}}(\omega)\}$, i.e. by setting the Fermi velocities to unity and considering transitions between the total (traced) spectral weight.

Rare-Earth vs. Heavy Metal Pigments and their Colors from First Principles – Supporting Information

Jan M. Tomczak
L. V. Pourovskii
L. Vaugier
A. Georges
S. Biermann

These supporting notes give additional information concerning the calculation of color of CeSF and HgS. In particular, we (a) describe the technical details of our computational scheme, “LDA+DMFT”, the combination of density functional theory within the local density approximation (LDA) with dynamical mean field theory (DMFT), (b) present the momentum resolved electronic structure and optical conductivity of our target compounds CeSF and HgS, (c) provide further evidence for our interpretation of the onset of optical transitions in CeSF being determined by p - f transitions by discussing the implications on the electronic structure and optical properties that would result from an alternative “ f - d scenario”, (d) summarize the Kubelka-Munk theory, which allows us to deduce the color of our compounds from the knowledge of the bulk optical conductivity, including practical details of our intermediate length scale modelisation. We conclude with a discussion of the *shape* of the onset of the absorption spectrum for the two prototypical compounds that we investigate, the quasi-two-dimensional CeSF with its localized f -electrons and the three-dimensional, more conventional HgS with broad and well-hybridising bands.

COMBINED DENSITY FUNCTIONAL AND DYNAMICAL MEAN-FIELD SIMULATIONS OF CESF

Our combined density functional and dynamical mean field “LDA+DMFT” implementation [1, 2] is based on a full-potential linearized augmented plane waves (LAPW) technique as implemented in the Wien2k code [3]. Our calculations are fully self-consistent, including over the charge density [4]. Spin-orbit coupling has been taken into account through a second variational treatment.

The LDA+DMFT calculations for CeSF have been carried out for the paramagnetic phase at the experimental crystal structure [5]; it is of tetragonal symmetry (space group $P4/nmm$), with the lattice parameters $a=3.993\text{\AA}$ and $c=6.950\text{\AA}$. The correlated f orbitals are constructed from projected atomic orbitals which are promoted to Wannier function through an orthonormalisation pro-

cedure. In practice, we have used an energy window $[-8 : 10.8]$ eV, which includes bands with mainly f orbital character, following the method implemented for d electron materials in Ref. [1]. Local correlations between the Ce $4f$ states have been treated within DMFT. The Hubbard and Hund interactions, $U = 4.8$ eV and $J = 0.70$ eV, resulting from the local Coulomb interaction on the Ce $4f$ shell, have been calculated within the constrained Random Phase Approximation (cRPA) [6]. We have employed the recent implementation of cRPA into the LAPW framework of the Wien2k code of Refs. [7, 8].

The Hubbard-I approximation has been employed as a quantum impurity solver within the LDA+DMFT scheme. We have used the full four-index Coulomb interaction matrix in the Hubbard-I impurity solver, thus all multiplet effects within the Ce $4f$ shell were taken into account. Double counting (DC) of Coulomb interactions between the f electrons was avoided, using the fully-localized limit (FLL) expression $\Sigma_\sigma = U(N-1/2) - J(N/2 - 1/2)$, where $N \approx 1$ is the occupancy of the Ce $4f$ shell in the DMFT quantum impurity problem[9]. In the self-consistent LDA+DMFT calculations we employed 225 k -points in the irreducible part of the tetragonal Brillouin zone (BZ) for the BZ-integration. All calculations have been carried out at the temperature of 116 K with a grid of 1024 Matsubara points, a high-frequency expansion up to the tenth order in $1/(i\omega_n)$ has been employed to describe tails of the Green’s function and the self-energy at Matsubara frequencies above the cutoff.

The local density approximation leads to a rather significant, yet expected, underestimation of the semiconducting gap between S $3p$ and lanthanide $5d$ bands in the rare-earth fluorosulfides. The LDA+DMFT approach employed in this work does not contain corrections for this LDA error, which is due to long-range interactions and the missing derivative discontinuity in the Kohn-Sham band structure. In addition, CeSF contains a partially filled localized $4f$ shell, and as pointed out in the main text, the relative positions of S $3p$, Ce $5d$ and Ce $4f$ states define the color of the material. In order to evaluate the effect of long-range interactions on the relative position of S $3p$ and Ce $5d$ bands we have performed one-shot calculations within Hedin’s GW approximation[10, 11] – using the implementation described in detail in Refs. [12, 13] – for CeSF and, for sake of comparison, for LaSF. For the latter, the optical gap is known to open between the valence S $3p$ and conduction La $5d$ bands. The band gap in LaSF calculated within the LDA is equal to 1.3 eV compared to the experimental optical gap of 2.8 eV [5]. Within the GW approximation, the value of the gap is increased by about 1.17 eV compared to the LDA one, and, hence, the LDA error is compensated by about 80%. As in usual semiconductors, the shape of the highest valence and lowest conduction bands, which are crucial for the absorption

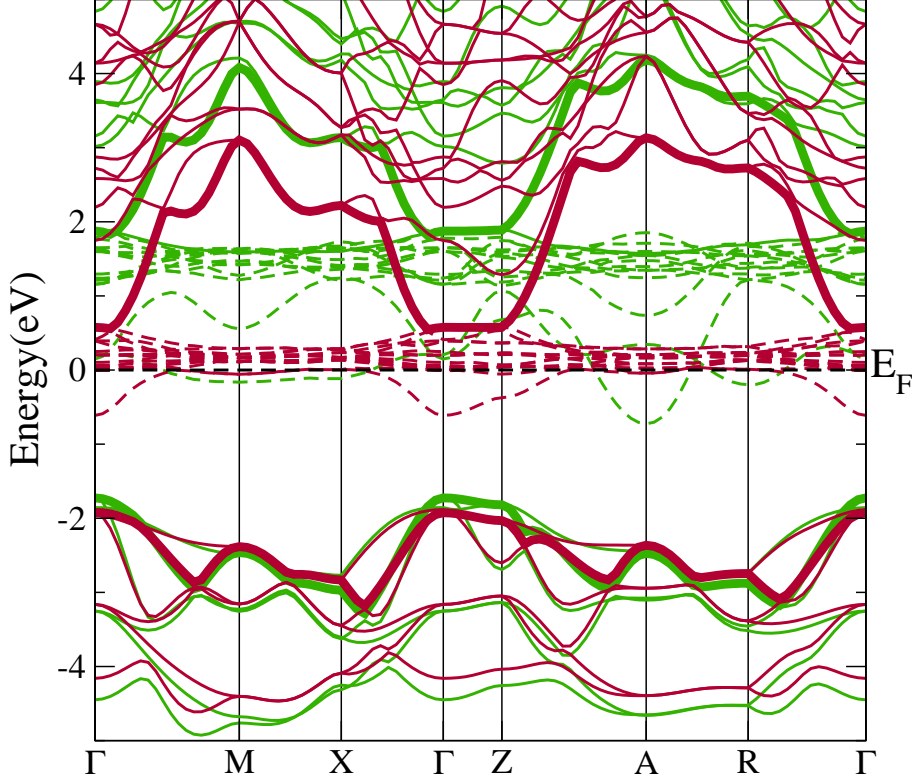


FIG. 6: The band structure of CeSF in LDA and GW . Band-structure of CeSF obtained within LDA (in red) and GW (in green). The Ce $4f$ states were treated as valence states in both cases. The bands of Ce $4f$ character are shown by dashed lines. The topmost S $3p$ and lowest Ce $5d$ bands are highlighted by fat lines. One may clearly see that the GW correction affects the Ce $5d$ bands much more strongly than S $3p$ ones.

edge, are barely affected by GW corrections.

We have performed similar GW simulations[12, 13] for CeSF, and the resulting $GW\mathbf{k}$ -resolved spectral function is compared to the LDA band structure in Fig. 6. As expected, the GW method is not able to describe correctly the strongly-correlated Ce $4f$ states, which remain metallic with their bandwidth increased relative to the LDA one. The important thing to notice here is that the upward shift for the bands of Ce $5d$ character relative to E_F is approximately 6 times larger than the corresponding (mostly downward) shift of the S $3p$ bands. Therefore, one may conclude that the underestimation of the pd-gap in this case is mainly an effect of the missing derivative discontinuity in the Kohn-Sham description, and thus a too low position of the $5d$ conduction states. As in the case of LaSF, the shape of the topmost valence and lowest conduction bands is weakly affected by GW corrections, and can be well described as a rigid shift of the corresponding bands. The value of the gap between those states is increased by about 1.15 eV, similarly to the case of LaSF.

On the basis of our GW simulations we conclude that,

in the case of CeSF, corrections to the Kohn-Sham band structure of the “uncorrelated” $3p$ - and $5d$ -bands and thus the relative positions of the CeSF bands relevant for its absorption edge – can be well described by a rigid shift of the Ce $5d$ states relative to Ce $4f$ and S $3p$ by a value close to the LDA band gap underestimation in LaSF. Hence, we have applied a static shift of 1.5 eV to the Kohn-Sham eigenvalues for unoccupied states with respect to the occupied bands and partially occupied Ce $4f$ states in our LDA+DMFT simulations of CeSF.

THE LDA+DMFT \mathbf{k} -RESOLVED SPECTRAL FUNCTION FOR CESF

The \mathbf{k} -resolved spectral function $A_{\mathbf{k}}(\omega)$ encodes the excitation energies associated with the addition or removal of an electron on top of the many-body ground-state Φ_0 :

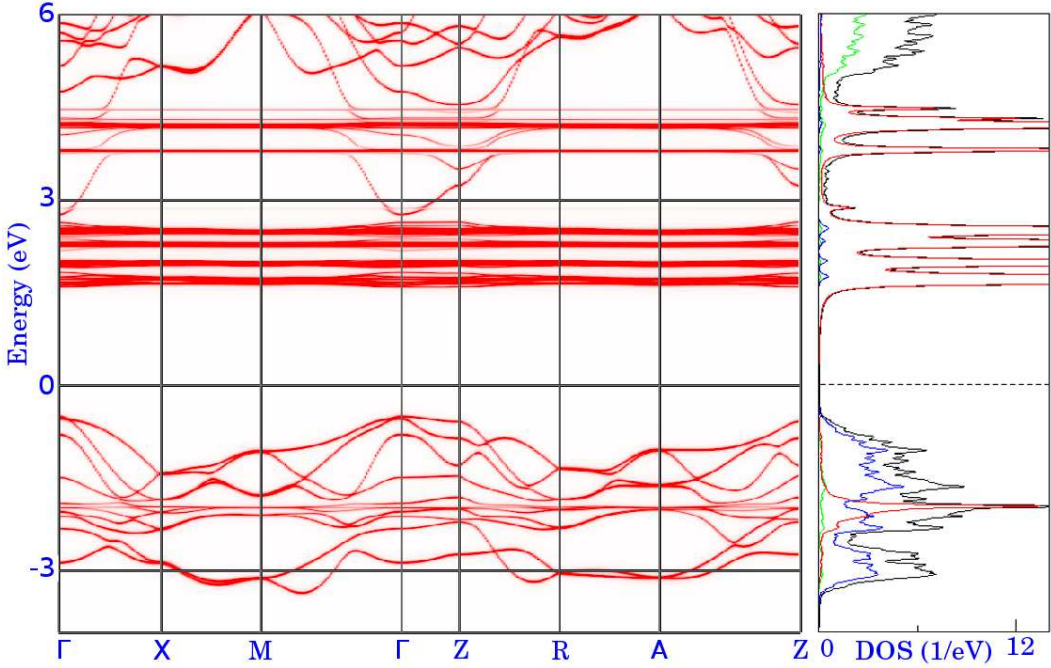


FIG. 7: **The LDA+DMFT excitation spectrum.** k -resolved spectral function (left panel) and the total (black), partial Ce $4f$ (red), Ce $5d$ (green), S $3p$ (blue) density of states (right panel) for CeSF

$$A_{\mathbf{k}}(\omega) = \sum_{\Gamma} \left\langle \Phi_{\Gamma} \left| c_{\mathbf{k}} \right| \Phi_0 \right\rangle^2 \delta(E_{\Gamma} - E_0 + \omega + \mu) + \sum_{\Gamma} \left\langle \Phi_{\Gamma} \left| c_{\mathbf{k}}^{\dagger} \right| \Phi_0 \right\rangle^2 \delta(E_0 - E_{\Gamma} + \omega + \mu), \quad (4)$$

where the sum runs over all excited many-body states Φ_{Γ} , μ is the chemical potential. When correlations are absent the many-body states Φ_0 and Φ_{Γ} are just Slater determinants, and the corresponding excitation energies are one-electron energies of the corresponding Hartree-Fock (or Kohn-Sham) problem.

In the framework of LDA+DMFT and in the basis of Kohn-Sham eigenstates the spectral function $A_{\mathbf{k}}(\omega)$ reads:

$$A_{\mathbf{k}}(\omega) = -\frac{1}{\pi} \text{Im} \left[\text{Tr} (\omega + i\eta + \mu - \hat{\epsilon}_{\mathbf{k}} - \Sigma_{\mathbf{k}}(\omega))^{-1} \right], \quad (5)$$

where $\hat{\epsilon}_{\mathbf{k}}$ is the diagonal matrix of Kohn-Sham eigenstates, $\Sigma_{\mathbf{k}}(\omega)$ is the DMFT local self-energy upfolded into the basis of Kohn-Sham eigenstates [1] (due to this upfolding it acquires \mathbf{k} -dependence) and η is a positive infinitesimal. When correlations beyond DFT are not included ($\Sigma = 0$) the \mathbf{k} -resolved spectral function has δ peaks at Kohn-Sham eigenvalues that form one-electron Kohn-Sham bands. In the case of metallic systems with weak or moderate correlations the Kohn-Sham eigenvalues are shifted and the corresponding δ peaks broad-

ened due to quasi-particle renormalization and life-time effects, respectively. In the present case of strongly-correlated Ce $4f$ states the DMFT self-energy leads to the destruction of coherent metallic $4f$ states and the formation of lower and upper Hubbard bands, hence opening the semiconducting gap.

The \mathbf{k} -resolved spectral function of CeSF along the $M - \Gamma - Z - R$ path in the Brillouin zone is shown in Fig. 1 of the main text. In Fig 7 we show the LDA+DMFT spectral function for CeSF for a longer ($\Gamma - X - M - \Gamma - Z - R - A - M$) path along with the corresponding integrated spectral function.

BAND-STRUCTURE CALCULATION OF HGS

For cinnabar red, α -HgS, we calculate, as a first step, the Kohn-Sham band-structure within the local density approximation (LDA), using the Wien2k[3] package. The crystal structure of α -HgS is hexagonal, with space group $P3_211$, 3 formula units per cell, and lattice constants $a=4.145\text{\AA}$ and $c=9.496\text{\AA}$ [14] [42].

The resulting band-structure is shown in figure 8 (a). We find an indirect gap of 1.3eV (from valence bands near the A-point to the conduction band at Γ), and an optical (=direct) gap of 1.33eV at the Γ -point. These findings are consistent with earlier results using the generalized gradient approximation.[15] Owing to the well-established underestimation of insulating gaps within

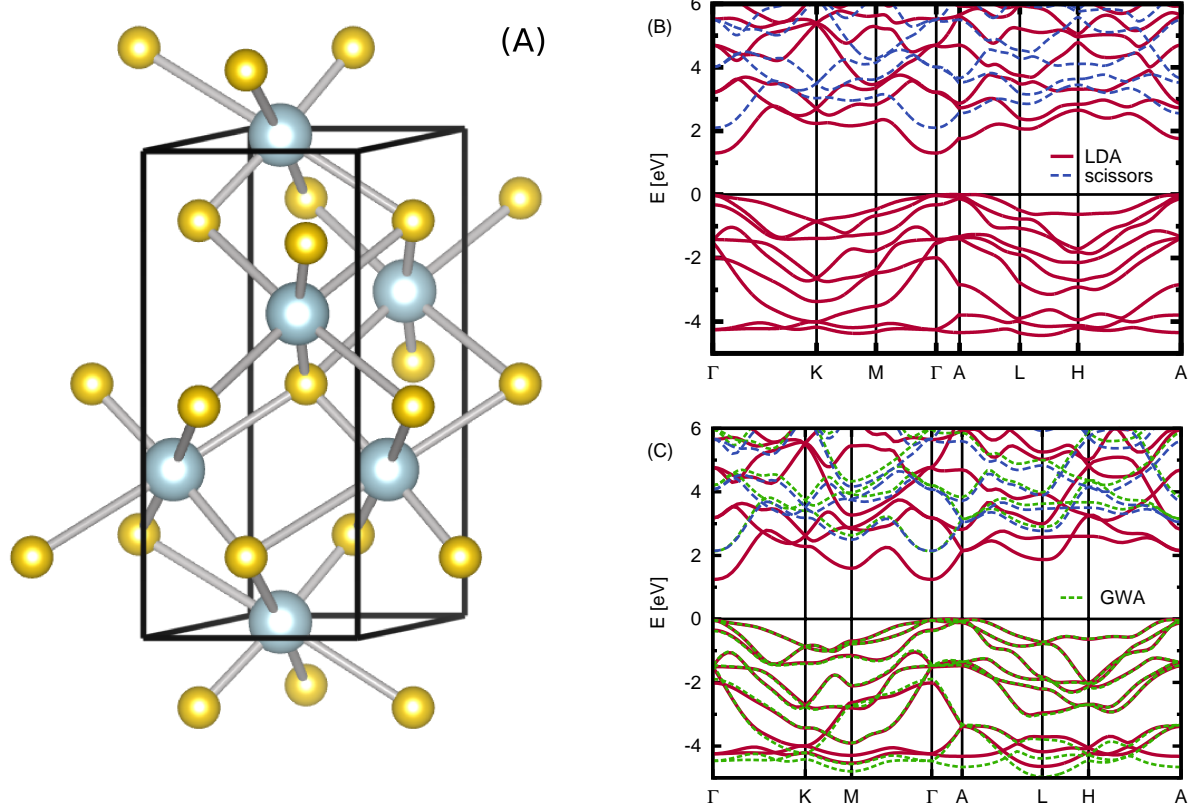


FIG. 8: **Crystal and band-structure of α -HgS.** (A) crystal structure of α -HgS (mercury atoms in blue, sulfur in yellow, graphic produced with Ref [21]). (B)-(C) Shown are results of (i) DFT-LDA using Wien2k (red, panel (B)) and FPLMTO (red, panel (C)), (ii) the GW approximation (green, panel (B)), and (iii) rigidly shifted (“scissors operator”) LDA conduction bands (blue : Wien2k, panel (B) : FPLMTO).

density functional theory, these values are much smaller than the experimental optical gap of ~ 2.1 eV[16].

In these cases it has become customary (see e.g. the recent Ref. [17]) to employ a scissors operator to tune the gap to its experimental value, before proceeding with the determination of e.g. optical properties. However, this procedure is *ad hoc* and would deprive us of our claim of performing *ab initio* calculations. Therefore, we went a step further and applied the GW approximation[18] to HgS. GW , a true many-body approach, has proved to be a valuable tool for moderately correlated systems, and is particularly suited to correct band-gaps in semiconductors[10, 11] (See also our paragraph on GW applied to CeSF in these supporting information).

For technical reasons, we resorted to a different electronic structure technique, the full potential linear muffin tin orbital (FPLMTO) method[19]. Using again the LDA potential, the FPLMTO band-structure, shown (in red) in figure 8 (b) is in reasonable agreement with our results using Wien2k. Taking these FPLMTO findings as starting point, we performed a one-shot GW calculation

using the code of Ref.[20].

The resulting quasi-particle band-structure [as obtained in the usual way of perturbing the Kohn-Sham eigenvalues to linear order in frequency in the GW self-energy[10]] is shown (as the green dashed lines) in figure 8 (b). The indirect gap comes out to be 2.1eV, in excellent agreement with experiment[16]. In the occupied part, this GW band-structure closely follows the LDA result for energies larger than -2eV. In the figure are also shown (in blue) the LDA conduction bands rigidly shifted upwards by a constant value. Evidently, with this scissors operation also the conduction bands of the LDA yield a favorable approximation to the GW results over at least 1eV of the bandwidth of unoccupied states. Therewith the “scissored” LDA covers an energy range sufficient to account for the onset of optical absorption.

With this *ab initio* justification, we turn back to the Wien2k data and apply a scissors operator to reproduce the GW gap, yielding an optical gap of 2.13eV. The resulting shifted conduction bands are shown (again in blue) in figure 8 (a). This establishes the band-structure

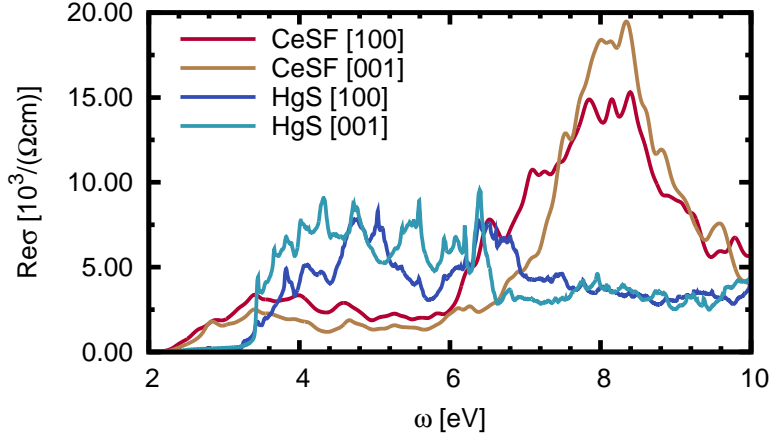


FIG. 9: **Optical conductivities of CeSF and HgS.** Shown are data over a wider energy range, and for different light polarizations with respect to the crystallographic axes.

that our calculations of the optical conductivity of HgS are based on.

It is worth mentioning that the onset of optical absorption takes place between bands of mainly S3p character for the valence band and Hg6s with admixtures of Hg6p and S3p for the conduction band.

OPTICAL CONDUCTIVITIES

In the main text, we showed the low energy onset of absorption in the polarization averaged optical conductivity. Owing to the non-cubic crystal structures (CeSF: tetragonal, HgS: hexagonal) there is a dependence of the optical response on the orientation of the light polarization with respect to the crystallographic axes. Figure 9 displays our results resolved into the two inequivalent orientations (along the crystallographic a and c-axis), as well as for an expanded energy range. In both compounds, the polarization dependence is notable mostly at higher energies. In the case of α -HgS we find an overall agreement with the dielectric function of Ref. [17]

We further would like to comment on our assumption that excitonic effects are negligible in the compounds considered, thus verifying our methodology (For a general discussion of these effects see Ref. [11]).

In conventional semiconductors, excitonic effects are well-known to severely modify absorption spectra through the appearance of sharply defined bound states below the conduction bands (see e.g. Ref. [22] for the example of SiO_2). Such features are absent in the experimental dielectric function of both HgS[17], and CeSF[28]. Besides, the electron-hole attraction in the excitonic regime may red-shift the onset of absorption (See e.g. Ref. [23] for a discussion on GaAs). Since we obtain good

values for the charge gaps for both HgS and CeSF, however, we believe this effect to be minor. Of course there can be effects of cancellation, e.g. in the case of HgS, between the electron-hole interaction induced redshift, and a potential gap *over-estimation* within GW . However, experience shows that LDA based one-shot GW calculations correct well for underestimations of LDA band-gaps, and rarely yield a too large gap with respect to experiment[20].

F-D INTRA-ATOMIC SCENARIO FOR THE ABSORPTION EDGE IN CESF: ELECTRONIC STRUCTURE

Similarly to many other Ce-based semiconductors (for example, the sesquioxide Ce_2O_3 [24], or the sesquisulfide Ce_2S_3 [25–27]) the absorption edge in CeSF has been previously ascribed to the Ce intra-atomic $4f$ to $5d$ transitions[5]. We will call this the “*f-d* scenario”, in contrast to the true “*p-f*” scenario established by our GW calculations for CeSF (see above). As discussed in the present manuscript, our LDA+DMFT calculations lead thus to a rather different picture of the CeSF electronic structure, with the onset of absorption being due to optical transitions between the occupied S 3p and empty Ce 4f bands, which result in a sharp absorption edge and the bright red color of this compound.

However, we have also simulated the optical properties and the coloration for CeSF in the “*f-d* scenario” by using the following procedure: starting from our LDA band structure described above, we apply an artificial upward shift of 1.5 eV to the partially filled Ce 4f band. This choice is in contradiction to the results of our GW simulations, see Sec. of this supporting information, but mimicks the situation of other ceria where a gap opens between *f* and *d* bands. The resulting “*f-d*” electronic

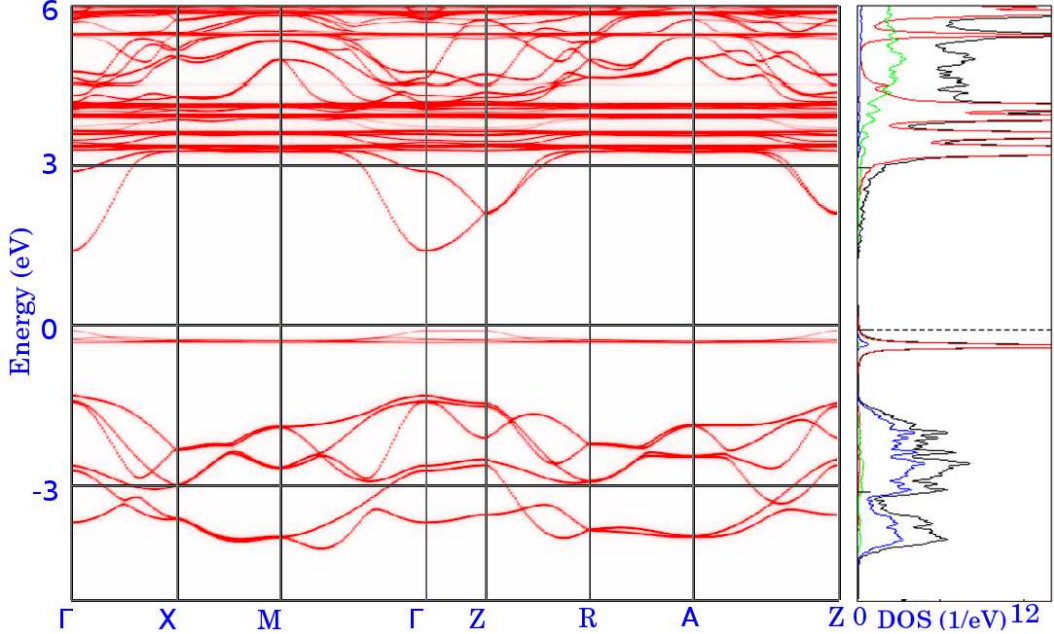


FIG. 10: **The *f-d* scenario.** The LDA+DMFT band structure of CeSF (left panel) obtained in the *f-d* scenario. Right panel: the corresponding total (black), partial Ce 4*f* (red), Ce 5*d* (green), S 3*p*(blue) density of states

structure is depicted in Fig. 10.

In this case the occupied Ce 4*f* band is located well above the top of the S 3*p* band, hence the absorption edge is due to Ce 4*f*-Ce 5*d* “intra-atomic” transitions. The calculated value of the band gap is 1.52 eV, which is smaller than the experimental one. Of course, the gap value depends on the choice of the shift. However, the sharpness of absorption edge is not sensitive to this parameter. One may notice, that, in agreement with previous electronic structure calculations [28], the bottom of the conduction band is very dispersive. Therefore, one should expect a rather slow growth of the joint density of states right above the gap.

Here, we verify this qualitative analysis and demonstrate that the “*f-d*” scenario fails to account for the established usability of CeSF as a high quality red pigment. Shown in figure 11 (a) and (b) are the (polarization averaged) optical conductivities and absorption coefficients for both scenarios. The gaps in both setups differ by several 100meV, explaining the different energies at which optical absorption sets in. The other major difference in the optical spectra is that the intensity in the “*f-d* scenario” is significantly lower than for the “*p-f*” scenario suggested by our *GW* calculations (see above). Indeed, the absorption coefficient $K(\omega)$ shown in figure 11 (b) fails to pass our quality measure for good pigments even in the bulk limit (concentration $c = 100\%$) : $K(\omega)$ surpasses $\beta/8$ (with $\beta = 50/\text{mm}$) at only about 0.2eV above the onset.

The consequences of this large variation in the sharp-

ness of the absorption onset are displayed in figure 12, which shows the diffuse reflectance and the resulting color for both scenarios (the detailed color coordinates are in Table 1 : The bulk color (see R_∞) is darker than the prominent orange/red of real CeSF that we reproduce in the “*p-f*” scenario. This mostly owes to the smaller value of the optical gap. As can be seen by looking at the red stimulus of the CIE observer, large parts of the red spectrum are cut off in the p-setup, decreasing the overall luminosity. The shallowness of the onset of absorption, causes admixtures of 5-10% of green and even blue, which slightly increases the brightness, but in a rather uniform fashion, i.e. mostly adding components of gray.

When using “*f-d*” CeSF as a realistic pigment, i.e. as a 20% admixture in a layer of $10\mu\text{m}$ on a white substrate, the color becomes a grayish ochre. This is due to the large increase in contributions from all colors, as is evident from the diffuse reflectance in figure 12. As expected from our analysis (based on our quality measure for the absorption coefficient), this instability with regard to the deployment in a realistic setup, i.e. the dependence of the color on the concentration and the film thickness, make “*f-d*” CeSF unsuitable for practical applications. This finding being at variance with the fact that CeSF is such a good pigment that it is indeed commercially used, thus strengthens our interpretation that in real CeSF the onset of absorption is due to *p-f* transitions, as described by our calculations.

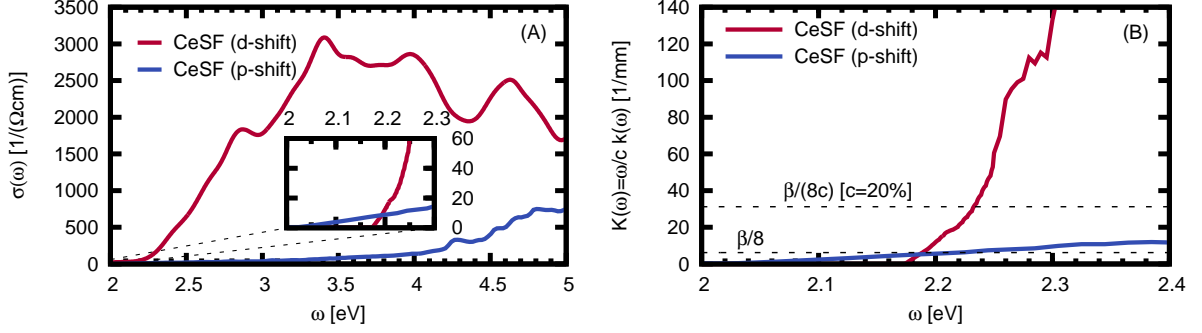


FIG. 11: **The two scenarios of CeSF : impact on the optical conductivity and the absorption coefficient.** Comparison of the (true) “*p-f*” the (artificial) “*f-d*” scenario for (A) the optical conductivity and (B) the absorption coefficient. The quality measure $\beta/8c$ in the right panel uses again $\beta = 50/\text{mm}$.

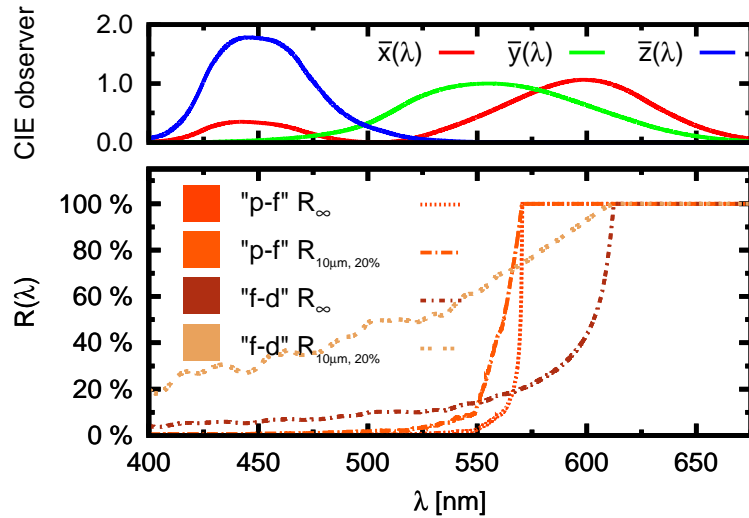


FIG. 12: **The theoretical diffuse reflectance.** Comparison of the diffuse reflectance $R(\lambda)$ and the corresponding colors in the “*p-f*” and the “*f-d*” scenario.

	thickness	concentration	X	Y	Z	x	y
CeSF “ <i>p-f</i> ” scenario	∞	100%	0.60	0.39	0.00	0.60	0.39
	∞	20%	0.63	0.44	0.01	0.58	0.41
	10 μm	20%	0.65	0.47	0.01	0.57	0.42
CeSF “ <i>f-d</i> ” scenario	∞	100%	0.36	0.26	0.01	0.50	0.37
	∞	20%	0.55	0.50	0.28	0.42	0.37
	10 μm	20%	0.74	0.73	0.44	0.39	0.38
HgS	∞	100%	0.53	0.33	0.01	0.67	0.33
	∞	20%	0.60	0.44	0.08	0.54	0.39
	10 μm	20%	0.65	0.52	0.08	0.52	0.42

TABLE I: **The colors of CeSF within the (true) “*p-f*” and the (artificial) “*f-d*” scenario, and HgS.** Shown are the CIE 1931 tristimulus values XYZ and the chromaticities xy ($z=1-x-y$) of both compounds, for different polarizations, pigment concentrations and sample thicknesses on a white substrate.

THE COLOR OF MATTER

The color of a pigment, or any object in general, owes to its diffuse, i.e. non-directional, reflectance. This has to be contrasted to the specular reflectivity of geometric optics as given by Fresnel's formulae. While the latter is entirely determined by the absorption properties of the system (for an application to colors and correlated materials see Ref. [29, 30]), the diffuse reflectance requires the accounting for the scattering of light due to imperfections of the specimen, such as impurities, grain boundaries or granularities. These are, by definition, effects that are beyond a first principles description of extended, perfect solids. We therefore resort to a modelisation for objects that both absorb and scatter light, where the latter is accounted for by an effective scattering rate β . While the latter in principle depends (like the absorption coefficient) on the frequency of the light, we shall demonstrate, for the case of CeSF, that this dependence is weak and non-essential for the fidelity of the calculated color.

Effective medium theory for light scattering in inhomogeneous media – the Kubelka-Munk model

The model that we employ for our calculations is owing to Kubelka and Munk[31, 32], and is based on considering two light fluxes, J_+ and J_- , that account for light propagating along a coordinate x downwards or upwards in a film of thickness L deposited on a substrate of reflectance R_S .

Using the absorption coefficient $K = \frac{\omega}{c} \text{Im}(n + ik) = \frac{\omega}{c} k$ and introducing the effective scattering parameter β , the differential fluxes follow (for details see e.g. Refs. [33, 34]) :

$$\frac{dJ_+(x)}{dx} = -2KJ_+(x) - \beta(J_+(x) + J_-(x)) \quad (6)$$

$$\frac{dJ_-(x)}{dx} = 2KJ_-(x) + \beta(J_+(x) + J_-(x)) \quad (7)$$

From this, we obtain for the reflectance $R(x) = -J_+(x)/J_-(x)$ at depth x

$$\frac{dR}{R} = \beta dx \left(R + \frac{1}{R} - 2 \left(1 + \frac{2K}{\beta} \right) \right) \quad (8)$$

integrating x from 0 to L , and thus R from $R(0) = R_S$, the substrate reflectance, to $R(L)$, and solving for $R(L)$ yields

$$R(L) = \frac{R_\infty^{-1}(R_S - R_\infty) - R_\infty(R_S - R_\infty^{-1})e^{\beta L(R_\infty^{-1} - R_\infty)}}{(R_S - R_\infty) - (R_S - R_\infty^{-1})e^{\beta L(R_\infty^{-1} - R_\infty)}} \quad (9)$$

where

$$R_\infty = \alpha - \sqrt{\alpha^2 - 1} \quad (10)$$

with $\alpha = 1 + 2K/\beta$ corresponding to the reflectance of a semi-infinite sample (bulk limit). Here, all quantities depend on the wavelength or frequency of the light. Using a pigment as an admixture to a (mostly transparent) host material can be modeled, in the simplest possible ansatz, by rescaling the absorption with the concentration c , i.e. using in the above equations cK instead of K .

The scattering parameter β

The above description on the diffuse reflectance relies on the scattering parameter β that is not accessible from first principle calculations for the perfect solid. In fact, β is a property that depends on the microstructure of the material. It arises thus the question of how to determine typical values of this parameter in practice, and, in particular, whether its frequency dependence is crucial for the calculation of the actual color.

In the case of CeSF there exist experimental measurements of both, the diffuse reflectance R [5] and the complex refractive index $\hat{n} = n + ik$ [28]. Assuming the validity of the KM model, equation (10) can thus be inverted to extract the scattering coefficient : $\beta_{KM} = \frac{2K}{\alpha-1}$, with α expressed as $\alpha = \frac{1}{2}(R + \frac{1}{R})$.

Fig. 13 shows R , K , and the resulting β_{KM} as a function of frequency. As it turns out, the frequency dependence of the scattering coefficient β is negligible. Indeed, approximating $\beta = 50/\text{mm}$ as indicated by the dashed line in figure 13, the reflectance R_{KM} within the KM model neatly traces the experimental data above the onset of absorption[43]. This justifies our choice to use the approximate $\beta(\omega) = 50\text{mm}^{-1}$ in all of our calculations. This value is moreover consistent with the range of values $\beta \approx 10 - 500\text{mm}^{-1}$ reported in the literature for a wide range of industrial inorganic pigments [35].

Opacity and covering power of thin films

A brilliant color of the bulk, as resulting from R_∞ , does not guarantee that a compound can be used as a pigment. While in some applications pigments are admixtures to the actual material the object is made of, pigments are mostly used in lacquer or paint. In other words it is not the bulk but the behavior in thin films, i.e. the opacity, that defines a good coloring material. Thus a good pigment must meet two requirements :

Imposing the pigment's color. The worst case is a "black" substrate : $R_S = 0$, while $R_\infty \neq 0$. Then it

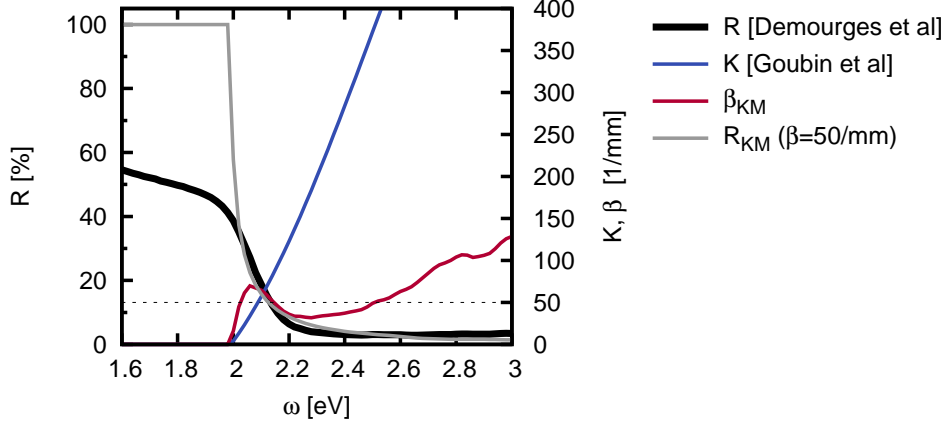


FIG. 13: **The diffuse reflectance.** Experimental diffuse reflectance R of CeSF from Demourges et al.[5], absorption coefficient $K = w/c \text{Im}\sqrt{\epsilon}$ from the dielectric function $\hat{\epsilon}$ of Goubin et al.[28], and scattering coefficient $\beta_{KM}(\omega)$, as extracted via the KM model. Also shown is the KM diffuse reflectance R_{KM} that results from the experimental absorption coefficient K and an energy-independent scattering coefficient $\beta = 50/\text{mm}$. The magnitude of the latter is indicated by the dashed line.

follows from equation (9)

$$R(L) = R_\infty \frac{e^{\beta L(R_\infty^{-1} - R_\infty)} - 1}{e^{\beta L(R_\infty^{-1} - R_\infty)} - R_\infty^2} \leq R_\infty \quad (11)$$

As a matter of fact the finite thickness of the film results, for the current case, in a more sharply defined absorption : While $R(L) = 1$ for $R_\infty = 1$, $R(L) < R_\infty$ for $R_\infty < 1$.

Hiding the color of the substrate. Now the worst case is a “white” substrate : $R_S = 1$, while $R_\infty \ll 1$. Then

$$R(L) = \frac{1 + R_\infty e^{\beta L(R_\infty^{-1} - R_\infty)}}{R_\infty + e^{\beta L(R_\infty^{-1} - R_\infty)}} \quad (12)$$

In that case $R(L) \geq R_\infty$, which means that a finite film will have a broader tail in the reflectance and admixtures of wavelengths away from the absorption edge are larger than for the bulk material. Hence the quality measure of a pigment that we introduce in the main manuscript considers a white substrate.

From the diffuse reflectance to the perceived color

While many spectroscopic devices have been devised to analyse matter, the spectrometer most commonly used is the human eye : it sensors the response to incident light in a range from roughly $\lambda = 400$ to 700 nm, and the information gathered by the rods and cones of the retina are post-processed by our brain into a brightness and color sensation.

The calibration, or *color matching functions*, of the three types of cones, responsible for the color perception, can be empirically measured [36, 37] and used to setup a three-dimensional color space. Many variants of color

schemes exist, and they are basically related by a unitary transformations of their coordinates. In the present work, we employ the CIE 1931 XYZ color space [38, 39]. The corresponding matching functions, probing the response to red, green, and blue light, are denoted $\bar{x}(\lambda)$, $\bar{y}(\lambda)$ and $\bar{z}(\lambda)$, and are displayed in the top panel of Fig. 4 of the manuscript or, here, figure 12.

Knowing the reflectivity $R(\lambda)$ of a material or object (as e.g. in the bottom panel of Fig. 4 of the main text or, here, figure 12), and the spectral distribution $S(\lambda)$ of the light source, i.e. accounting for the type of light that the considered object is illuminated with, the XYZ color coordinates, or *tristimulus values*, are calculated as (see e.g. Ref. [40])

$$(X, Y, Z) = k \int d\lambda R(\lambda) S(\lambda) (\bar{x}(\lambda), \bar{y}(\lambda), \bar{z}(\lambda)) \quad (13)$$

where k is a normalization constant chosen such that $k \int d\lambda S(\lambda) \bar{y}(\lambda) = 1$. As light source we use in our calculations the CIE standard illuminant D65 [41], which is appropriate for usual day light. While the tristimulus coordinates include information on both color and brightness, in color pictograms often only the color information given by the normalized *chromaticity values*

$$\begin{aligned} x &= \frac{X}{X + Y + Z} \\ y &= \frac{Y}{X + Y + Z} \\ z &= \frac{Z}{X + Y + Z} \end{aligned} \quad (14)$$

which are shown in Table 1 for the two scenarios of CeSF, as well as for HgS.

INTERBAND ABSORPTION IN TWO-BAND MODEL

In order to understand how the topology of the bottom of conduction/top of valence bands in CeSF influences its optical properties we consider a simplified model, in which we include a single valence and a single conduction band with analytical dispersion laws. This model is adequate to describe the optical conductivity in the vicinity of the absorption edge, where the relevant interband transitions are between single valence and conduction bands, which have a quasi-two-dimensional shape in the case of CeSF (see Fig. 14b). Thus, to model the absorption edge in CeSF we consider the case of “cylindrical” valence and conduction bands (Fig. 14a). Three-dimensional (“spherical”) bands (Fig. 14c) provide a more adequate model of the actual states involved in optical transitions at the absorption edge of HgS (especially for the conduction band, see Fig. 14d).

In calculations of the interband absorption one starts from the real part of the optical conductivity (Eq. 1 in the main text), which in the case of zero temperature can be written as:

$$\text{Re}\sigma(\nu) = \frac{2\pi e^2 \hbar}{V} \sum_{\mathbf{k}} \int \frac{d\omega}{\nu} \text{tr}[v(\mathbf{k})A(\mathbf{k}, \omega)v(\mathbf{k})A(\mathbf{k}, \omega+\nu)]. \quad (15)$$

The imaginary part of the dielectric function (in CGS units) and absorption K are then evaluated from $\text{Re}\sigma(\omega)$ as

$$\text{Im}\epsilon^{cgs}(\omega) = \frac{4\pi}{\omega} \text{Re}\sigma^{cgs}(\omega) = \frac{\text{Re}\sigma(\omega)}{\omega\epsilon_0} \quad (16)$$

$$K(\omega) = \frac{\omega k(\omega)}{c} = \frac{\omega \text{Im}\epsilon^{cgs}(\omega)}{2\hat{n}c} = \frac{\text{Re}\sigma(\omega)}{2\hat{n}c\epsilon_0}, \quad (17)$$

where $\hat{n} = n + ik$ is the refractive index, c is the speed of light, ϵ_0 is the vacuum permittivity. The absorption $K(\omega)$ has the dimension of inverse length.

Neglecting the \mathbf{k} -dependence for the velocities, $v_{12}(\mathbf{k})v_{21}(\mathbf{k}) = -v^2$ one may carry out the energy integration in (15) and obtain the optical conductivity expressed through the “joint density of states”:

$$\begin{aligned} & \int d\omega \delta[\hbar\omega - E_v(\mathbf{k})] \delta[\hbar\omega - E_c(\mathbf{k}) + \hbar\nu] \\ &= \frac{1}{\hbar} \delta[E_v(\mathbf{k}) - E_c(\mathbf{k}) + \hbar\nu], \end{aligned} \quad (18)$$

where $E_v(\mathbf{k})$ and $E_c(\mathbf{k})$ are the valence and conduction bands dispersions, respectively. Then (15) reads as follows:

$$\text{Re}\sigma(\nu) = -\frac{2\pi e^2 \hbar}{\nu} v^2 \int \frac{2d^3k}{8\pi^3} \delta[E_v(\mathbf{k}) - E_c(\mathbf{k}) + \hbar\nu]. \quad (19)$$

Let us now introduce the band dispersions corresponding to the “spherical” (Fig. 14c)

$$E_v(\mathbf{k}) = -\frac{\hbar^2 k^2}{2m_v}, \quad (20)$$

$$E_c(\mathbf{k}) = \frac{\hbar^2 k^2}{2m_c} + \Delta, \quad (21)$$

and “cylindrical” (Fig. 14a)

$$E_v(\mathbf{k}) = -\frac{\hbar^2(k_x^2 + k_y^2)}{2m_v}, \quad (22)$$

$$E_c(\mathbf{k}) = \frac{\hbar^2(k_x^2 + k_y^2)}{2m_c} + \Delta, \quad (23)$$

cases. Here, $m_{v(c)}$ are the valence (conduction) band’s effective masses and Δ is the band gap value.

By substituting the d^3k integration in (19) with the integration over the constant energy surface $\int d^3k \delta[E(\mathbf{k}) - E_0] \dots \rightarrow \int \frac{dS}{\nabla_k [E(\mathbf{k}) - E_0]} \dots$ one obtains the real part of the optical conductivity:

$$\text{Re}\sigma^{sph}(\delta\omega) = \frac{2\sqrt{2}e^2v^2}{(\Delta + \hbar\delta\omega)\pi\hbar^2} m_r^{3/2} (\hbar\delta\omega)^{1/2}, \quad (24)$$

$$\text{Re}\sigma^{cyl}(\delta\omega) = \frac{2e^2v^2}{(\Delta + \hbar\delta\omega)a\hbar} m_r, \quad (25)$$

for the spherical and cylindrical dispersions, respectively. Here, m_r is the reduced effective mass $m_r = m_c m_v / (m_c + m_v)$. $\hbar\delta\omega$ is the photon energy relative to the absorption edge, $\hbar\nu = \Delta + \hbar\delta\omega$. Of course, $\text{Re}\sigma(\delta\omega) = 0$ within the gap ($\delta\omega < 0$), hence one may immediately see that $\text{Re}\sigma^{cyl}(\delta\omega)$ exhibit a jump at the absorption edge, while $\text{Re}\sigma^{sph}(\delta\omega)$ is continuous everywhere.

The corresponding absorptions (17) for $\delta\omega \geq 0$ (for $\delta\omega < 0$ the absorption is again zero) read

$$K_{sph}(\delta\omega) = \frac{\sqrt{2}e^2v^2}{\pi(\Delta + \hbar\delta\omega)\hat{n}\hbar^2c\epsilon_0} m_r^{3/2} (\hbar\delta\omega)^{1/2} \quad (26)$$

$$K_{cyl}(\delta\omega) = \frac{e^2v^2}{(\Delta + \hbar\delta\omega)a\hbar\hat{n}c\epsilon_0} m_r. \quad (27)$$

To model the CeSF case one may assume a flat conduction band (the dispersion of the Ce 4f states at the bottom of conduction band is negligible, see Fig. 14b), hence $m_r = m_v$. For the effective mass we used the value $m_r = m_v$ equal to $0.6m_0$, which was extracted from the curvature of the topmost S 3p band at Γ in the CeSF LDA+DMFT momentum-resolved spectral function, Fig. 7. Other parameters entering in Eqs. (26,27)

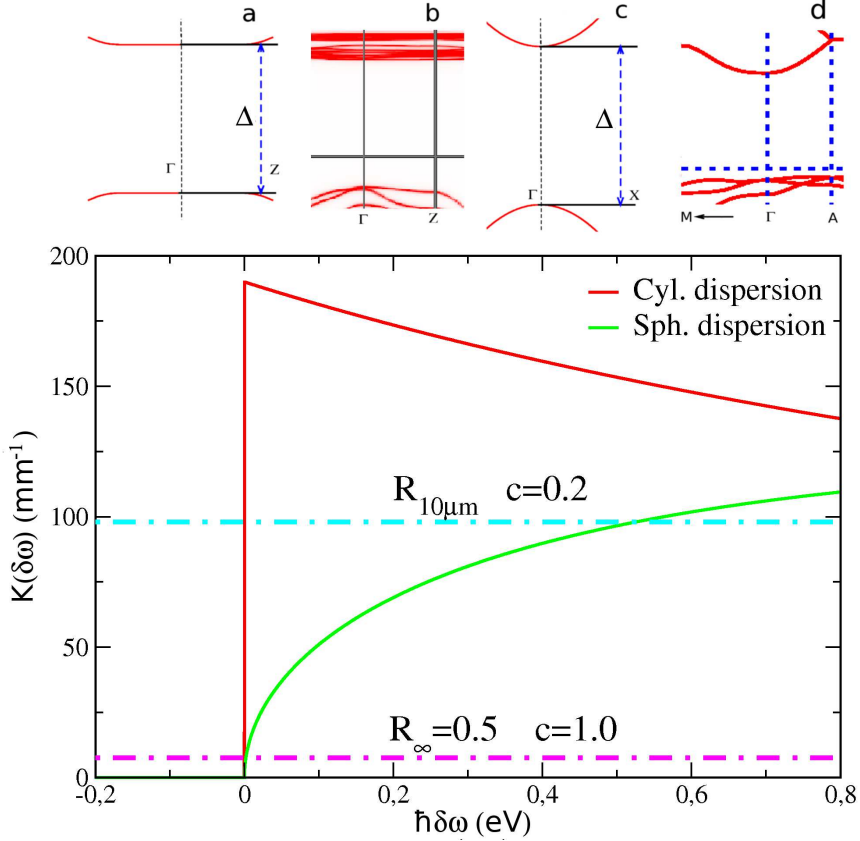


FIG. 14: Upper panel: a. Two model bands “cylindrical” along the $\Gamma - Z$ path (along other two paths $\Gamma - X$ and $\Gamma - Y$ they have the same shape as shown in c.); b. Zoom at the CeSF bands along the $\Gamma - Z$ path.; c. Two model bands in the spherical case; d. Zoom at the HgS bands along the $M - \Gamma - A$ path. Lower panel: Absorption $K(\delta\omega)$ for the two-band models with spherical and cylindrical band dispersions. The cyan and pink horizontal lines indicate the threshold value of K for the semi-infinite bulk and thin film cases, see the text

were chosen as follows: $\Delta=2.1$ eV, $\hat{n} \approx 2$ was obtained from the full complex optical conductivity of CeSF, the average Fermi velocity can be estimated to be $v = V_{pf} \cdot \delta_{Ce-S} \sim 0.3$ eV Å, where $\delta_{Ce-S} \approx 3$ Å is the distance between next-nearest Ce and S sites in CeSF, and V_{pf} is a hybridization matrix element between the involved orbitals.

The resulting absorptions for both the spherical and cylindrical cases are displayed in Fig. 14 with the same set of model parameters employed for both cases. One may see that the stepwise behavior of the curve in the “cylindrical” case results in a much higher absorption just above the edge as compared to the spherical case. This leads to an important difference in the color properties in the two cases. To quantify those properties we again employ the KM model with the scattering parameter $\beta = 50/\text{mm}$ and compute the characteristic absorption thresholds for the two cases considered in the article: the semi-infinite bulk of pure pigment and a thin layer of $10 \mu\text{m}$ with the pigment concentration $c = 0.20$. In the “spherical” case the characteristic absorption threshold

$\delta\omega_{1/2}$, for which the diffuse reflectance $R = 1/2$, is equal to ~ 7 meV for the semi-infinite bulk. Hence, the absorption edge is sufficiently sharp in this case. However, in the case of a thin film we obtain $\delta\omega_{1/2}=0.52$ eV, which is substantially larger than the characteristic frequency interval $\delta\omega_c \approx 0.2$ eV (see the main text). Therefore, the “model material” with the spherical bands (Fig. 14c) would hardly make a very good pigment. In contrast, in the model system with the two-dimensional band topology the diffuse reflectance will undergo a discontinuous transition from $R = 1$ to $R \approx 0$ exactly at the edge. Hence, a quasi two-dimensional topology of the conduction/valence bands naturally leads to a sharp onset of absorption and drop in R as predicted by the LDA+DMFT simulations for CeSF (see Fig. 4 in the main manuscript).

[1] Aichhorn, M. *et al.* Dynamical mean-field theory within an augmented plane-wave framework: Assessing elec-

- tronic correlations in the iron pnictide LaFeAsO. *Phys. Rev. B* **80**, 085101 (2009).
- [2] Ferrero, M., Parcollet, O. TRIQS: a Toolbox for Research in Interacting Quantum Systems. <http://ipht.cea.fr/triqs>.
- [3] Blaha, P., Schwarz, K., Madsen, G., Kvashnicka, D. & Luitz, J. *WIEN2k, An augmented Plane Wave + Local Orbitals Program for Calculating Crystal Properties* (Techn. Universität Wien, Austria, ISBN 3-9501031-1-2., 2001).
- [4] Aichhorn, M., Pourovskii, L. & Georges, A. Importance of electronic correlations for structural and magnetic properties of the iron pnictide superconductor LaFeAsO. *Phys. Rev. B* **84**, 054529 (2011).
- [5] Demourgues, A., Tressaud, A., Laronze, H. & Macaudiere, P. Rare earth fluorosulfides LnSF and Ln₂AF₄S₂ as new colour pigments. *J. Alloys and Comp.* **323-324**, 223–230 (2001).
- [6] Aryasetiawan, F. *et al.* Frequency-dependent local interactions and low-energy effective models from electronic structure calculations. *Phys. Rev. B* **70**, 195104 (2004).
- [7] Vaugier, L., Jiang, H. & Biermann, S. Hubbard U and Hund's exchange J in transition metal oxides: Screening vs. localization trends from constrained random phase approximation. *Phys. Rev. B* **86**, 165105 (2012).
- [8] Vaugier, L. *Electronic Structure of Correlated Materials From First Principles: Hubbard interaction and Hund's exchange*. Ph.D. thesis, Ecole Polytechnique (France).
- [9] Pourovskii, L. V., Amadon, B., Biermann, S. & Georges, A. Self-consistency over the charge-density in dynamical mean-field theory: a linear muffin-tin implementation and some physical implications. *Phys. Rev. B* **76**, 235101 (2007).
- [10] Aryasetiawan, F. & Gunnarsson, O. The GW method. *Rep. Prog. Phys.* **61**, 237–312 (1998).
- [11] Onida, G., Reining, L. & Rubio, A. Electronic excitations: density-functional versus many-body Green's-function approaches. *Rev. Mod. Phys.* **74**, 601–659 (2002).
- [12] Jiang, H., Gomez-Abal, R. I., Rinke, P. & Scheffler, M. Localized and itinerant states in lanthanide oxides united by GW@LDA+U. *Phys. Rev. Lett.* **102**, 126403 (2009).
- [13] Jiang, H., Gomez-Abal, R. I., Rinke, P. & Scheffler, M. First-principles modeling of localized d states with the GW@LDA+U approach. *Phys. Rev. B* **82**, 045108 (2010).
- [14] Auvray, P. & Genet, F. Affinement de la structure cristalline du cinabre α -HgS. *Bulletin de la Société Française de Minéralogie et de Cristallographie* **96**, 218 (1973).
- [15] Sun, S.-R., Li, Y.-C., Liu, J., Dong, Y.-H. & Gao, C.-X. Electronic structures and metallization of HgS under high pressures: First principles calculations and resistivity measurements. *Physical Review B (Condensed Matter and Materials Physics)* **73**, 113201 (2006).
- [16] Choe, S.-H., Yu, K.-S., Kim, J.-E., Park, H. Y. & Kim, W.-T. Optical properties of HgS and HgS:Co²⁺ crystals. *J. Mater. Res.* **6**, 2677 (1991).
- [17] Cardona, M. *et al.* Electronic and phononic properties of cinnabar: Ab initio calculations and some experimental results. *Phys. Rev. B* **82**, 085210 (2010).
- [18] Hedin, L. New method for calculating the one-particle Green's function with application to the electron-gas problem. *Phys. Rev.* **139**, A796–A823 (1965).
- [19] Methfessel, M., van Schilfgaarde, M. & Casali, R. A full-potential LMTO method based on smooth Hankel functions. *in Electronic Structure and Physical Properties of Solids: The Uses of the LMTO Method, Lecture Notes in Physics*. H. Dreyssse, ed. **535**, 114–147 (2000).
- [20] Kotani, T., van Schilfgaarde, M. & Faleev, S. V. Quasi-particle self-consistent GW method: A basis for the independent-particle approximation. *Phys. Rev. B* **76**, 165106 (2007).
- [21] Momma, K. & Izumi, F. VESTA 3 for three-dimensional visualization of crystal, volumetric and morphology data. *J. Appl. Crystallogr.* **44**, 1272–1276 (2011).
- [22] Chang, Eric K. & Rohlfing, M. & Louie, S. G. Excitons and Optical Properties of α -Quartz. *Phys. Rev. Lett.* **85**, 2613–2616 (2000).
- [23] Rohlfing, M. & Louie, S. G. Electron-Hole Excitations in Semiconductors and Insulators. *Phys. Rev. Lett.* **81**, 2312–2315 (1998).
- [24] Golubkov, A. V., Prokof'ev, A. & Shelykh, A. I. Optical characteristics of Ce₂O₃ single crystals. *Phys. Solid State* **37**, 1028 (1995).
- [25] Dagys, R., Babonas, G.-J. & Pukinskas, G. Optical and magneto-optical properties of (La_{1-x}Ce_x)₂S₃ crystals. *Phys. Rev. B* **51**, 6995–6998 (1995).
- [26] Witz, C., Huguenin, D., Lafait, J., Dupont, S. & Théye, M. Comparative optical studies of Ce₂S₃ and Gd₂S₃ compounds. *JOURNAL OF APPLIED PHYSICS* **79**, 2038–2042 (1996).
- [27] Windiks, R., Wimmer, E., Pourovskii, L., Biermann, S. & Georges, A. Structure and optical properties of α - and γ -cerium sesquisulfide. *Journal of Alloys and Compounds* **459**, 438 – 446 (2008).
- [28] Goubin, F. *et al.* The dielectric function of LnSF rare-earth fluorosulfides (Ln = La, Ce): experiment and theory. *J. Solid State Chem.* **117**, 2833–2840 (2004).
- [29] Tomczak, J. M. & Biermann, S. Optical properties of correlated materials - or why intelligent windows may look dirty. *Phys. Status Solidi B (feature article)* **246**, 1996 (2009).
- [30] Tomczak, J. M. & Biermann, S. Materials design using correlated oxides: Optical properties of vanadium dioxide. *Europhys. Lett.* **86**, 37004 (2009).
- [31] Kubelka, P. & Munk, F. Ein Beitrag zur Optik der Farbanstriche [A contribution to the optics of coats of paints]. *Zeits. f. Techn. Physik* **12**, 593–601 (1931). German.
- [32] Kubelka P (1948) New contributions to the optics of intensely light-scattering materials, part I. *J. Opt. Soc. Am.* 38:448–457.
- [33] Zuppiroli, L. & Bussac, M.-N. *Traité des couleurs* [A treatise on colours] (Presses Polytechniques et Universitaires Romandes (PPUR), 2001). French.
- [34] Levinson, R., Berdahl, P. & Akbari, H. Solar spectral properties of pigments, part I. *Solar Ener. Mat. Solar Cells* **89**, 319–349 (2005).
- [35] Levinson, R., Berdahl, P. & Akbari, H. Solar spectral properties of pigments, part II. *Solar Ener. Mat. Solar Cells* **89**, 351–389 (2005).
- [36] Wright, W. D. A re-determination of the trichromatic coefficients of the spectral colours. *Transactions of the Optical Society* **30**, 141–164 (1929).
- [37] Guild, J. The colorimetric properties of the spectrum. *Philosophical Transactions of the Royal Society of London. Series A* **230**, 149 (1932).

- [38] CIE. *Commission internationale de l'Eclairage proceedings [Proceedings of the International Commission on Illumination]*, 1931 (Cambridge University Press, Cambridge, 1932). French.
- [39] Smith, T. & Guild, J. The C.I.E. colorimetric standards and their use. *Transactions of the Optical Society* **33**, 73–134 (1931).
- [40] Nassau, K. *The Physics and Chemistry of Color: The Fifteen Causes of Color*, 2nd Edition (Wiley Series in Pure & Applied Optics, 2001).
- [41] S005/E-1998, J. S. I. C. *CIE standard illuminants for colorimetry* (ISO/CIE, 1999).
- [42] In our calculation we neglect the spin-orbit coupling, since its influence at low energy was found to be small[17].
- [43] Below the onset of absorption, the reflectance of the KM model is, by construction, always 100%. The difference to the experimental reflectance is owing to residual in-gap absorption, that, like the scattering coefficient, is beyond an *ab initio* description of the perfect solid.